Pergamon

Int. J. Heat Mass Transfer. Vol. 41, No. 2, pp. 475–487, 1998

Printed in Great Britain
0017–9310/98 $19.00+0.00

PII: S0017-9310(97)00137-3

Analysis of flow and heat transfer in twin-roll strip casting process

JEE-GONG CHANG and CHENG-I WENG†

Department of Mechanical Engineering, National Cheng Kung University, Tainan, Taiwan, Republic of China

(*Received* 2 *August* 1996 *and in final form* 10 *January* 1997)

Abstract—The twin-roll process is modeled by a coupled fluid flow and phase change model by means of a versatile finite element method. The multidomain method is employed to deal with the solid and liquid phases separately, which includes treating the liquid phase as an Newtonian fluid and the solid phase as a viscoplastic metal. Furthermore, a simple and efficient method is used for overcoming the difficulty of remesh phase encountered during iteration. From the results of this study, the inlet region must be included in the analysis for obtaining the reliable flow field within the strip. In addition, the circulation occurs in the molten region and it is driven mainly by the rotating rollers. Finally, the interface position and shape are both influenced by the inlet flow rate and angular speed of rollers. © 1997 Elsevier Science Ltd.

INTRODUCTION

In twin-roll casting process, molten metal is fed through a tip into the cavity formed by the walls of two rotating rolls, which are water cooled from the inside. The molten metal solidifies and forms a thin shell on rolls surface, since heat is extracted by the chilled rolls. Immediately after the complete solidification, the metal is rolled before reaching the nip. A schematic diagram of this process is depicted in Fig. 1. Apparently, this process consists two major processes of a conventional steel mill, namely casting and rolling process. The integration of the two processes also offer further savings in energy and manufacturing costs by eliminating some of the intermediate stages, such as soaking, loading, conveying, and unloading. Furthermore, twin-roll casting can produce better properties due to high cooling rate. However, the twin-roll process requires a more sophisticated control system than other conventional rolling processes [1, 2]. Knowledge of the strip fluid flow and heat transfer behavior are essential for proper quality control of the product.

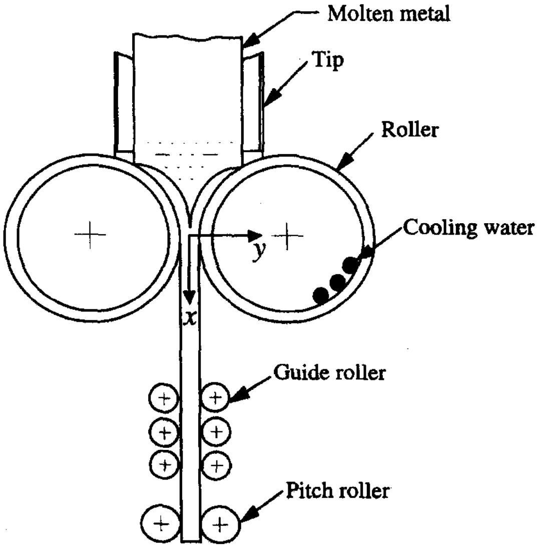

Fig. 1. Schematic diagram of twin-roll caster.

Over the past decade, several contributions have been made in modeling the twin-roll casting process. Miyazawa *et al.* [3] developed a mathematical model to evaluate the effects of several operational parameters such as the angular velocity of the rolls, the feed rate of the material, etc. and found that there exists only a narrow range of these parameters affording stable operation. The velocity field was obtained by an analytical method under the assumptions of the small clearance between two rollers and disregarding the inertia effect. However, these two assumptions are somehow far from the real physical situation. Saitoh *et al.* [4] applied this method to obtain the velocity field and used the boundary fixing method to handle the heat transfer problem by means of a complicated coordinate transformation. Karabin *et al.* [5, 6] thermal-mechanical model to predict certain measurable process parameters. However, the temperature was obtained only coupled with the mechanical field in a consistent way. Takuda *et al.* [7] obtained the velocity field only fulfilling the kinematic conditions and the temperature field was obtained in decoupling with the velocity field. However, in twin-roll casting, the flow field has a significant effect on the solidification process itself and on the metallurgical structure of the strip. All afore-mentioned literature really provided a

---

† Author to whom correspondence should be addressed.

NOMENCLATURE

$\mathbf{b}$	body force vector
c	specific heat
$\mathbf{C}$	advection matrix
$\mathbf{d}$	generalized displacement vector
$\mathbf{D}$	diffusion matrix
$\mathbf{E}$	strain rate tensor
$\mathbf{f}$	force vector
h_0	height of the outlet
h_1	height of the inlet
h_e	effective heat transfer coefficient
$\mathbf{I}$	three by three identity matrix
k	thermal conductivity
L	latent heat
$\mathbf{M}_P$	pressure mass matrix
$\mathbf{n}$	unit normal vector
p	pressure
Q	flow rate
$\mathbf{Q}$	gradient matrix
R	radius of roll
T	temperature
T_{in}	temperature of the inlet
T_m	melting temperature
T_∞	ambient temperature
$\mathbf{t}$	unit tangent vector
u, v	velocities in x- and y-directions, respectively
$\mathbf{v}$	velocity vector
x, y	Cartesian coordinates.

Greek symbols

α	relaxation coefficient
$\dot{\bar{\varepsilon}}$	effective strain rate
ψ, w, φ, ϕ, ϑ	weighting function
Γ_i, Γ_c, Γ_T	interface, convection and traction force boundaries, respectively
λ	penalty number
μ	viscosity
ρ	density
$\bar{\sigma}$	effective stress
$\boldsymbol{\sigma}$	stress tensor
σ_Y	yielding stress
τ_x	x-component of traction force
ω	rotating speed
Ω	modelling domain
Ω_e	element domain
ξ, η	coordinates in calculating domain.

Superscript

n	iteration level.

Subscripts

h	discretized
l	liquid phase
s	solid phase
U	velocity aspect
T	temperature aspect.

deep insight into the fundamental phenomenon of twin-roll casting interacting with the operational parameters, however, from the viewpoint of design a more accurate and appropriate model is required for obtaining more valuable information to avoid the trial-and-error efforts at intermediate stages of development. The appropriate models taking into account the inertia effect and the coupling of fluid flow and heat transfer are provided until recent years with the progress of the numerical methods and techniques. Ha *et al.* [8] employed the control volume method to simulate the unsteady twin-roll casting and assumed the molten metal to be filled at initial state. Hwang *et al.* [9] simulated the filling sequences at the start-up stage of the process. Hwang *et al.* [10] analysed the effect of various process variables of a twin-roll caster with a feeding nozzle by employing the enthalpy method in a steady state. However, a restrictive assumption of the flat surface between two rollers at the inlet is made. This, somehow, may introduce some inaccuracies to the flow field of the molten liquid metal.

The main object of this study is to use the versatile finite-element method to simulate the twin-roll casting process. The multidomain method is employed to deal with the solid and liquid phases separately, which includes treating the liquid phase as a Newtonian fluid and the solid phase as a viscoplastic metal and problem is solved by the coupled fluid flow and heat transfer model. The numerical methods used here are based on the author's previous work [11] and the newly implemented numerical algorithm for overcoming the difficulty arising from the improvement of the physical model is also included. The effect of various process parameters on the thermal and flow behavior are examined.

MATHEMATICS FORMULATION

The geometry of an idealized twin-roll process is depicted in Fig. 2. The two-dimensional model is based of on the assumption that the ratio of the width to thickness is large and hence the side board effect is neglected. In addition, the process is also assumed to be in a steady state, and the buoyancy effects are negligible, due to the fact that molten metal is mainly driven by the roller rather than by gravity [12]. The governing equations, simulating the twin-roll process for the both liquid and solid phases, include the continuity, momentum, and energy equations, and are described as follows:

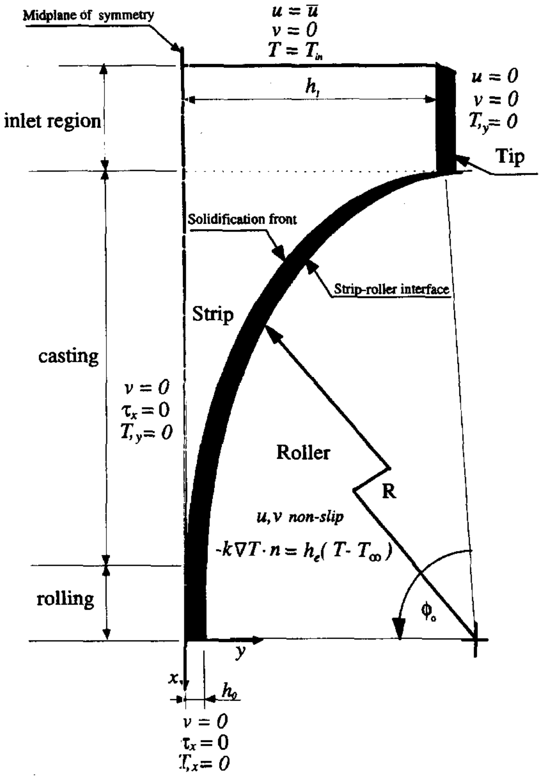

Fig. 2. Idealized geometry of simulation domain and boundary conditions.

$$\nabla \cdot \mathbf{v} = 0 \tag{1}$$

$$\rho \mathbf{v} \cdot \nabla \mathbf{v} - \nabla \cdot \boldsymbol{\sigma} = \rho \mathbf{b} \tag{2}$$

$$\rho c \mathbf{v} \cdot \nabla T = \nabla \cdot (k \nabla T) \tag{3}$$

where $\mathbf{v}$ is the velocity vector with u and v its components in the x- and y-direction; ρ is the density; $\boldsymbol{\sigma}$ is the stress tensor; $\mathbf{b}$ is the body force vector; c is the heat capacity; T is the temperature; and k is the conductivity.

The constitutive equation is

$$\boldsymbol{\sigma} = -p\mathbf{I} + 2\mu(\sigma_Y, \dot{\bar{\varepsilon}}, T)\mathbf{E} \tag{4}$$

where p is the pressure; $\mathbf{I}$ is the 3×3 identity matrix; μ is the viscosity; σ_Y is the yield stress; $\dot{\bar{\varepsilon}}$ is the effective strain rate; and $\mathbf{E} = 1/2[\nabla \mathbf{v} + (\nabla \mathbf{v})^T]$ is the strain rate tensor.

In equation (4), μ is generally a function of yield stress, effective strain rate, and temperature. In addition, μ plays an important role in modeling different kinds of material behavior, such as Newtonian fluid, non-Newtonian polymer, and viscoplastic metal, covering both liquid phase and solid phase [13, 14]. In the present approach, different forms of μ is used to model the molten and solidified metals, and it is described in the following.

In liquid phase the viscosity is assumed to be independent of temperature, i.e μ = constant. In solid phase, the viscoplastic model of Perzyna type is used to simulate the behavior of solidifying metal from liquid to solid as well as the solid at high temperature, and the viscosity can be expressed in the following form [15]:

$$\mu = \frac{1}{3}\frac{\bar{\sigma}}{\dot{\bar{\varepsilon}}} \tag{5}$$

where $\bar{\sigma}$ is the effective stress, and $\dot{\bar{\varepsilon}}$ is the effective strain rate. Note that in the present analysis an expression of effective stress as a function of effective strain rate and temperature (i.e. $\bar{\sigma} = c(T)\dot{\bar{\varepsilon}}^{m(T)}$) is provided by uniaxial compression test [16] and thus the final expression of the viscosity of the solid is shown in the Table 1.

The associated boundary conditions for the above governing equations are described as follows:

At the inlet, the velocity profile is assumed as a quadratic function of y which is under the assumption of the plane Poiseuille flow with a sufficiently long

Table 1. Physical properties of stainless steel and operational parameters for calculation [4, 9, 16]

Physical property	Symbol	Unit	SUS 304
Thermal conductivity (solid)	k_s	$\mathrm{W\,m^{-1} \cdot K^{-1}}$	31.90
Thermal conductivity (liquid)	k_l	$\mathrm{W\,m^{-1} \cdot K^{-1}}$	20
Specific heat (solid)	c_s	$\mathrm{kJ\,kg^{-1} \cdot K^{-1}}$	0.644
Specific heat (liquid)	c_l	$\mathrm{kJ\,kg^{-1} \cdot K^{-1}}$	0.67
Density	$\rho_l = \rho_s$	$\mathrm{kg\,m^{-3}}$	7400
Latent heat	L	$\mathrm{kJ\,kg^{-1}}$	272.2
Melting temperature	T_m	°C	1400
Roll diameter	$2R$	cm	8.9
Half of strip thickness	h_0	cm	0.16
Flow rate	Q	$\mathrm{cm^2\,s^{-1}}$	0.4
Angle of roll bite	ϕ_0	deg	43
Viscosity (liquid)	μ	$\mathrm{N \cdot s\,m^{-2}}$	0.56
(solid)	$\mu = \frac{1}{3}c\dot{\bar{\varepsilon}}^{m-1}$	$\mathrm{N \cdot s\,m^{-2}}$	
where	$c = 718.92 \times e^{6371.6344/T}$	$\mathrm{N \cdot s^m\,m^{-2}}$	
and	$m = -4.2875^{-6} \times T^2 + 0.0088775 \times T - 4.225$		

inlet length and thus the fully developed profile is obtained, and the inlet temperature is assumed to be uniform, we have

$$u = \frac{3}{2}\frac{Q}{h_1}\left[1-\left(\frac{y}{h_1}\right)^2\right] \tag{6}$$

$$v = 0 \tag{7}$$

$$T = T_{\mathrm{in}} \tag{8}$$

where Q is the flow rate and h_1 is the height of the inlet.

Along the tip surface, the non-slip condition is applied and thermal insulated condition is assumed, hence

$$u = 0 \tag{9}$$

$$v = 0 \tag{10}$$

$$\frac{\partial T}{\partial y} = 0 \tag{11}$$

At solidification front, the mass conservation in the normal direction, non-slip condition in the tangential direction, fixed melting temperature under phase change, and the energy conservation across the interface are applied. Here, the assumption of existing only one solid/liquid interface is made, that is the effect of the mushy zone is neglected. Generally speaking, the effect of the mushy zone is mainly dependent on the magnitude of the difference between the solidus and liquidus temperature and cooling condition of the process. The related boundary conditions are described as follows:

$$\rho_s \mathbf{v}_s \cdot \mathbf{n} = \rho_l \mathbf{v}_l \cdot \mathbf{n} \tag{12}$$

$$\mathbf{v}_s \cdot \mathbf{t} = \mathbf{v}_l \cdot \mathbf{t} \tag{13}$$

$$T = T_{\mathrm{m}} \tag{14}$$

$$k_l \nabla T_l \cdot \mathbf{n} - k_s \nabla T_s \cdot \mathbf{n} = \rho L \mathbf{v} \cdot \mathbf{n} \tag{15}$$

where the subscript s and l represent the solid and liquid phases; **n** and **t** are the unit normal and tangent vector of the solidification front; T_{m} is the melting temperature; L is the latent heat of solidification, the effect of which is the cause of the temperature gradient discontinuity across the interface.

At the interface of strip and roller surface, the non-slip condition, based on the observation of experiment [17], is assumed; and the heat convection model represented by the effective heat transfer coefficient and the ambient temperature is used to replace the actual heat transfer between strip and roller. Two parameters can be used to represent the cooling capability of the roller, hence we have

$$u = \omega\sqrt{R^2 - x^2} \tag{16}$$

$$v = \omega x \tag{17}$$

$$-k\nabla T \cdot \mathbf{n} = h_e (T - T_\infty) \tag{18}$$

where ω is the rotational speed and R is the radius of the roller; h_e is the effective heat transfer coefficient between the roller and strip.

At the outlet, it is assumed that heat conduction in x-direction is negligible, and vanishing of the velocity in y-direction and the normal traction, hence we have

$$v = 0 \tag{19}$$

$$\tau_x = 0 \tag{20}$$

$$\frac{\partial T}{\partial x} = 0. \tag{21}$$

At the midplane of symmetry conditions and the vanishing of tangential traction are used, hence we have

$$v = 0 \tag{22}$$

$$\tau_x = 0 \tag{23}$$

$$\frac{\partial T}{\partial y} = 0. \tag{24}$$

FINITE ELEMENT METHOD

The methodology of the finite element formulation used here is mainly based on the authors' previous works [11]. the same formulation, thus, is just described briefly, except the newly implemented numerical algorithm. The weak form of the continuity, momentum, and energy equations can be obtained by using the weighted residuals method. The discrete weak formulation involves applying the test functions ψ to equation (1), and $\mathbf{w}$, φ to equation (2) and equation (3) where ψ is also chosen as the interpolation of pressure and $\mathbf{w}$, φ can be chosen as different from interpolation function of velocity and temperature, and using the divergence theorem; the liquid phase formulation is combined with the solid phase formulation by incorporating the interfacial boundary condition of the latent heat released under phase change as stated in equation (15). After obtaining the resulting equation, the consistent penalty [18, 19] is used to eliminate the pressure variable for the sake of reducing the total degrees of freedom of the final matrix. Moreover, this method can provide more accurate results than the penalty method, in which the technique of reduced integration is incorporated, when deal with more complex geometry or isoparameteric meshes. Finally, the derived equations are

$$\int_\Omega [\rho \mathbf{v}\cdot(\nabla \mathbf{v})\mathbf{w} + \lambda(\nabla_{\mathrm{h}}\cdot\mathbf{v})(\nabla_{\mathrm{h}}\cdot\mathbf{w}) + 2\mu\mathbf{E}:\nabla\mathbf{w}]\,\mathrm{d}\Omega = \int_\Omega \rho\mathbf{b}\cdot\mathbf{w}\,\mathrm{d}\Omega + \int_{\Gamma_{\mathrm{T}}} (\sigma)\mathbf{w}\cdot\mathbf{n}\,\mathrm{d}\Gamma \tag{25}$$

$$\int_{\Omega} [k\nabla T\cdot\nabla\varphi+\rho c(\mathbf{v}\cdot\nabla T)\varphi]\,\mathrm{d}\Omega$$

$$= -\int_{\Gamma_i}\rho L(\mathbf{v}\cdot\mathbf{n})\varphi\,\mathrm{d}\Gamma-\int_{\Gamma_c}h(T-T_\infty)\varphi\,\mathrm{d}\Gamma \quad (26)$$

where Ω is the modeling domain containing both liquid and solid phases and Γ_i, Γ_c and Γ_T correspond to the melt/solid, convective, and traction boundaries respectively. The symbol ":" denotes the dyadic product, ∇_h is a discrete divergence operator introduced by Engelman *et al.* [19] and λ, a large number, is the penalty number. Note that the pressure space still appears explicitly in the penalty formulation, equation (25), this is the main difference between the present method and penalty method accompanied with the technique of reduced integration.

A new element [20, 21] is used to interpolate the velocity and pressure with biquadratic and linear functions respectively, as depicted in Fig. 3. The main advantages of using this element are that it provides a superior characteristic of convergence than other element and the yield no spurious pressure mode in the solution. The interpolation functions for velocity and temperature are introduced as

$$\mathbf{v} = \sum_{i=1}^{9}\mathbf{v}_i\phi_i, \quad T = \sum_{i=1}^{9}T_i\phi_i \quad (27)$$

at element level (i.e. Ω_e), where $\mathbf{v}_i$ and T_i are unknown nodal values of velocity and temperature. The interpolation functions for p are introduced as

$$\psi_1 = \frac{1}{3}+\frac{\sqrt{2}}{\sqrt{3}}\eta, \quad \psi_2 = \frac{1}{3}-\frac{1}{\sqrt{2}}\xi-\frac{1}{\sqrt{6}}\eta,$$

$$\psi_3 = \frac{1}{3}-\frac{1}{\sqrt{2}}\xi-\frac{1}{\sqrt{6}}\eta \quad (28)$$

where ξ and η are the coordinates defined in the calculating domain.

The test function is chosen as different from the interpolation function, as in the well-known Petrov–Galerkin method, in order to suppress oscillating solutions existing in the convective dominant problem. The upwinding is achieved by defining the weighting functions as follows:

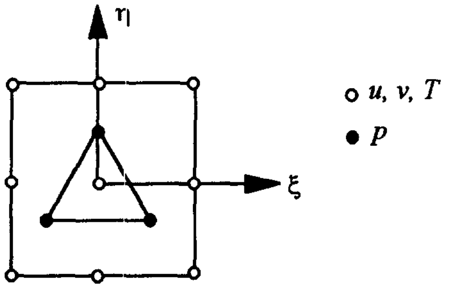

Fig. 3. A nine-node velocity and temperature, three-node pressure element.

$$\varphi_i = \phi_i(x,y)+\vartheta_i(x,y;\mathbf{v}), \quad w_i = \phi_i(x,y)+\vartheta_i(x,y;\mathbf{v}) \quad (29)$$

where ϕ is a Lagrangian biquadratic basis function. The extra function ϑ, suggested by Heinrich *et al.* [22], contains information about the direction and magnitude of the local velocity field.

The global equation can then be obtained by summing all the elements that construct the approximate space (i.e. $\Omega = \cup\,\Omega_e$). After substituting the interpolation functions into equations (25) and (26), the final matrix form at the element level can be obtained as

$$(\mathbf{C}_\mathrm{U}+\mathbf{D}_\mathrm{U}+\lambda\mathbf{Q}\mathbf{M}_\mathrm{p}^{-1}\mathbf{Q}^\mathrm{T})\mathbf{v} = \mathbf{f}_\mathrm{U} \quad (30)$$

$$(\mathbf{C}_\mathrm{T}+\mathbf{D}_\mathrm{T})\mathbf{T} = \mathbf{f}_\mathrm{T} \quad (31)$$

where **C** and **D** are the advection and diffusion matrices and the subscripts U and T represent velocity and temperature. $\mathbf{M}_\mathrm{P}$ is the pressure mass matrix containing the pressure interpolation functions, **Q** and $\mathbf{Q}^\mathrm{T}$ are the matrices associated with the gradient operator, and **f** is the forcing function and natural boundary condition. A detailed description of the above matrices and the derivation of finite equation can be seen in refs. [20] and [23].

The crucial point of the penalty method in practical computation is the determination of the penalty number, λ. Generally, the selection of λ depends on both viscous and inertia terms. In order to fulfill the incompressibility constrain, the penalty number must be large enough to make a distinct difference between $\mathbf{C}_\mathrm{U}$, $\mathbf{D}_\mathrm{U}$ and $\mathbf{Q}\mathbf{M}_\mathrm{p}^{-1}\mathbf{Q}^T$ matrices. However, too large a number will destroy the accuracy of solution, since only finite significant digits are carried in the computation. A comprehensive discussion in determination of λ can be seen in ref. [24]. Although, some empirical criteria for determining λ are available, it is still hard to determine it under some complicated situations, such as the viscosity varies in several orders of magnitude under phase change. The difficulty lies in the selection of λ cannot satisfy both considerations of machine accuracy and incompressibility constraint. For overcoming this problem, the iterative penalty method, namely Uzawa algorithm [25, 26], is used here and the procedure is briefly describe as follows:

(1) given $\mathbf{P}^{n-1}$, solve for $\mathbf{v}^n$ as

$$(\mathbf{C}_\mathrm{U}+\mathbf{D}_\mathrm{U}+\lambda\mathbf{Q}\mathbf{M}_\mathrm{p}^{-1}\mathbf{Q}^\mathrm{T})\mathbf{v}^n = \mathbf{f}_\mathrm{U}+\mathbf{Q}\mathbf{P}^{n-1}. \quad (32)$$

(2) update

$$\mathbf{P}^n = \mathbf{P}^{n-1}+\lambda\mathbf{M}_\mathrm{p}^{-1}\mathbf{Q}^\mathrm{T}\mathbf{v}^n. \quad (33)$$

(3) repeat steps 1 and 2 until the discrete divergence,

$$\mathrm{DIV}_h = \max_{\mathrm{nel}}|\mathbf{Q}^\mathrm{T}\mathbf{v}^n_\mathrm{nel}| \quad (34)$$

is sufficiently small.

Note that the traditional penalty method corresponds to the case when $\mathbf{P}^{n-1}$ is zero and the iteration is performed only once. DIV_h is the maximum value of discrete divergence taken from over all

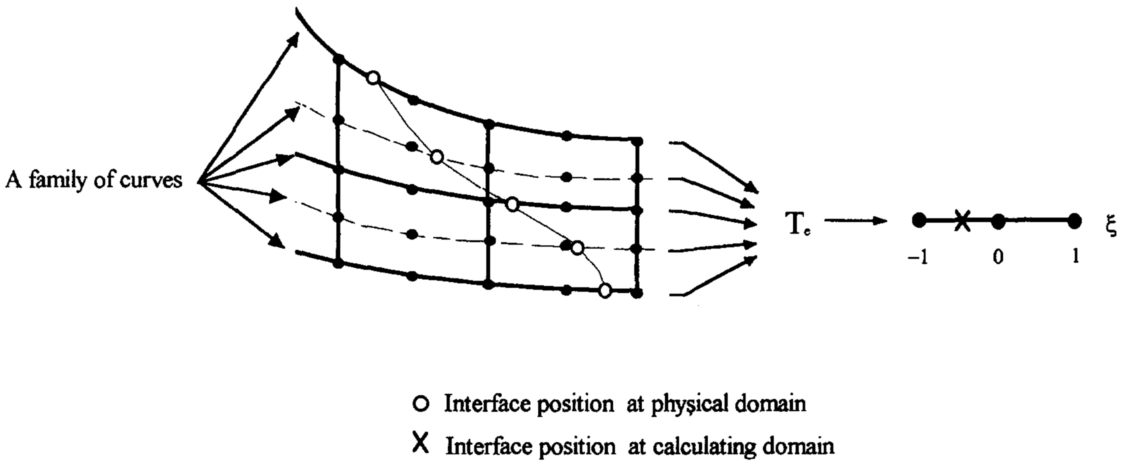

Fig. 4. Illustration of procedure of finding interface positions.

elements of the mesh. In addition, DIV_h also provides a useful information of satisfaction of a divergence-free velocity field and can be qualified as a powerful and versatile diagnostic tool. It also can be used in the traditional penalty and mixed methods for confirming the reliability of the solution. The major advantage of the Uzawa algorithm is that it guarantees satisfaction of the incompressibility constraint to desired accuracy for a moderately large penalty number. Thus, in practical computation, the magnitude of penalty number can be easily decided for just taking the minimum viscosity into account.

The direct successive iteration method is used to solve to nonlinear matrix algebra equations, (30) and (31), for validity over a wide range of nonlinearity. The successive iteration method, including updated the solution using an under-relaxation method, is given as:

$$\mathbf{d}^n = \alpha \mathbf{d}^n + (1-\alpha)\mathbf{d}^{n-1} \tag{35}$$

where **d** is the generalized displacement vector and can represent the velocity, temperature or interface position, α is the under-relaxation number, and the superscript n denotes iteration level. The iterations are performed separately in solving fluid-flow and heat-transfer problems. Note that when dealing with a nonlinear geometry problem, that the relative variation of interface position is smaller than a given tolerance is used as a stop criterion.

REMESH PHASE

Due to the satisfaction of continuity conditions within an element, the mesh must be updated during each iteration step to maintain the element boundary at the melt/solid interface for taking into account the discontinuities of temperature gradient and material properties across the melt/solid interface. The location of the melt/solid interface is found by using the melting point isothermal condition. In order to increase the efficiency of finding the interface position, a family of curves which remain unchanged throughout the computation is introduced, along with a set of mapping functions establishing the correspondence between the family of curves and the curvilinear coordinates defined in the calculating domain. The main advantage of this method lies in finding the interface position in one dimension rather than two, thus reducing the complexity of the remesh phase. In addition, the interface position is found not only at the lement boundary, but also in the interior of the element by mapping all nodes lying in the family of curves to the calculating domain. The procedure can be briefly summarised as depicted in Fig. 4, where interface position is successively found on the family of curves. The interface shape is interpolated by quadratic functions at the final element-level calculation, thus it is found as a curve rather than a line, offering more accuracy in both calculation of the area integral and latent heat line integral. The detailed procedure can be seen in ref. [11].

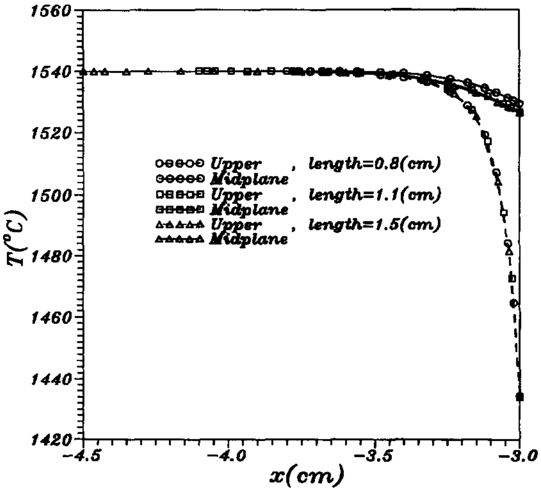

Fig. 5. Temperature distributions for different inlet lengths at $\omega = 0.3$ rad s^{-1}.

RESULTS AND DISCUSSION

The twin-roll process conditions of this study come from a laboratory scale caster and the material properties as well as the geometric data of the process are summarized in Table 1 [4, 9, 16]. In addition, the formulae related to the expression of viscosity, fitted from the experimental data, are also included in Table 1 [16]. Note that the viscosity of solid is both the functions of effective strain rate and temperature.

For the sake of easily analysing the flow field or saving the computing time, the inlet region is often neglected in previous works by the researchers [5–7]. Thus, the inlet boundary conditions are then applied artificially. However, these conditions have a significant influence on the results of flow field. Physically, we have a better knowledge on the upstream boundary conditions than those on the downstream. As a consequence, the computational domain is enlarged to cover the inlet region in present approach and a fully developed profile is assumed at the inlet. In order to access the correct enlarged length, the different inlet lengths are verified. From the results, as shown in Fig. 5, when the inlet length is increased to 1.1 cm the temperature, obtained near the regions formed by two rollers, along the inner surface of the tip and midplane are invariant as compared to that with the long inlet length. Thus, in the following analysis the inlet length is set as 1.1 cm due to the fact that this length is sufficiently long (for this length, the acceptable range of the rotational speed of the roller, ω, is up to 0.36 rad s^{-1} approximately). The initial finite element mesh topology is shown in Fig. 6(a), where the mesh contains 408 elements and 1725 nodes. The final mesh topology as the solution converged is shown in Fig. 6(c). As can be seen, the interface shape

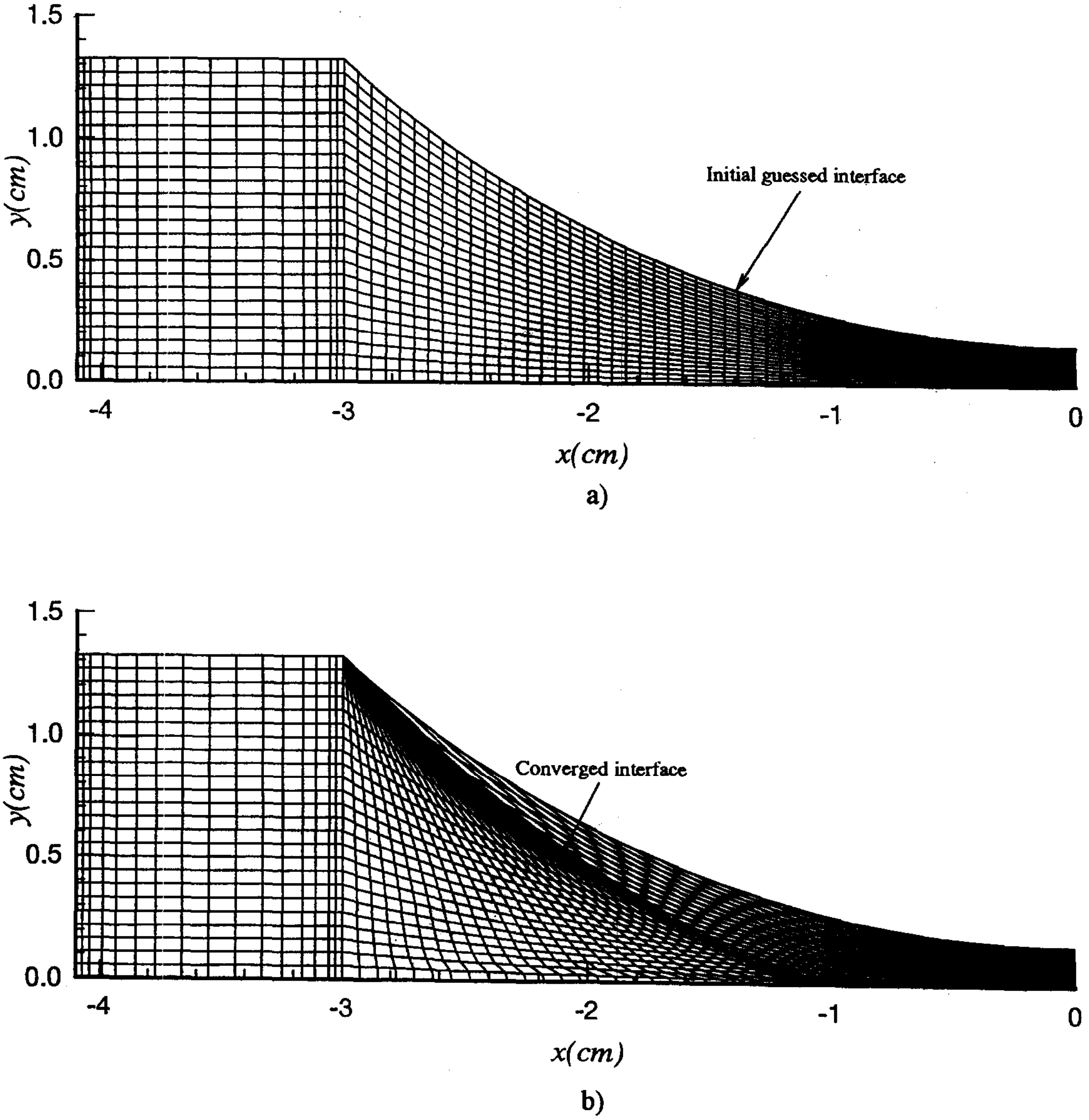

Fig. 6. Mesh topology of twin-roll casting process: (a) initial mesh; (b) final mesh.

is found as a curve rather than a line, and there is no need of the extra effort to interpolate the interface shape from the result of temperature. The illustrations of stream lines and temperature contours are also indicated in Figs. 7(a) and (b), respectively. From the results, a small circulation zone is formed in the liquid phase and the high-temperature gradient area occurs in the region near the roller.

Figures 8(a) and (b) show the velocity vector in the inlet region with different angular velocities of the roller, ω. The results indicate that the velocity of the inlet region is also influenced by the rotational speed of the roller. Owing to the drag force of the roller, the flow direction moves upward near the region formed by two rollers. In addition, both the magnitude and direction of the inlet velocity at $x = -3$ are influenced by the angular velocity of the roller, especially for the lower part of the beginning of the roll bite. Thus, it cannot be decided as a quadratic function of y or uniform at different ω when the inlet region is neglected in the analysis. Figure 9 shows the inlet temperature at $x = -3$ with different rotational speeds of the roller. The results also indicates the inlet temperature is function of the rotational speed of the roller. In addition, the inlet temperature is uniform at small rotational speed, except the upper part of the beginning of the roll bite. Thus, the uniform temperature can be used as an approximate inlet condition at small rotational speed of the roller when the inlet region is neglected in the analysis. The formation of the circulation as angular velocity of the roller increased is shown as in Figs. 10(a)–(d). From which it is seen that, the circulation zone enlarges as the angular velocity of the roller is increased. Besides, this circulation is mainly driven by the force convection rather than natural convection. The temperature contours, shown in Fig. 11 as $\omega = 0.36$ rad s^{-1}, are bent inward as compared to Fig. 7(b). The result also indicates the velocity field have a strong influence on the temperature distribution. The comparison of the temperature along the upper surface of the strip and midplane at the different rotational speeds of the roller is shown in Fig. 12. The temperature range between the upper surface of the strip and midplane shortens as the rotational speed of the roller is increased. This behavior is mainly due to the circulation to increase

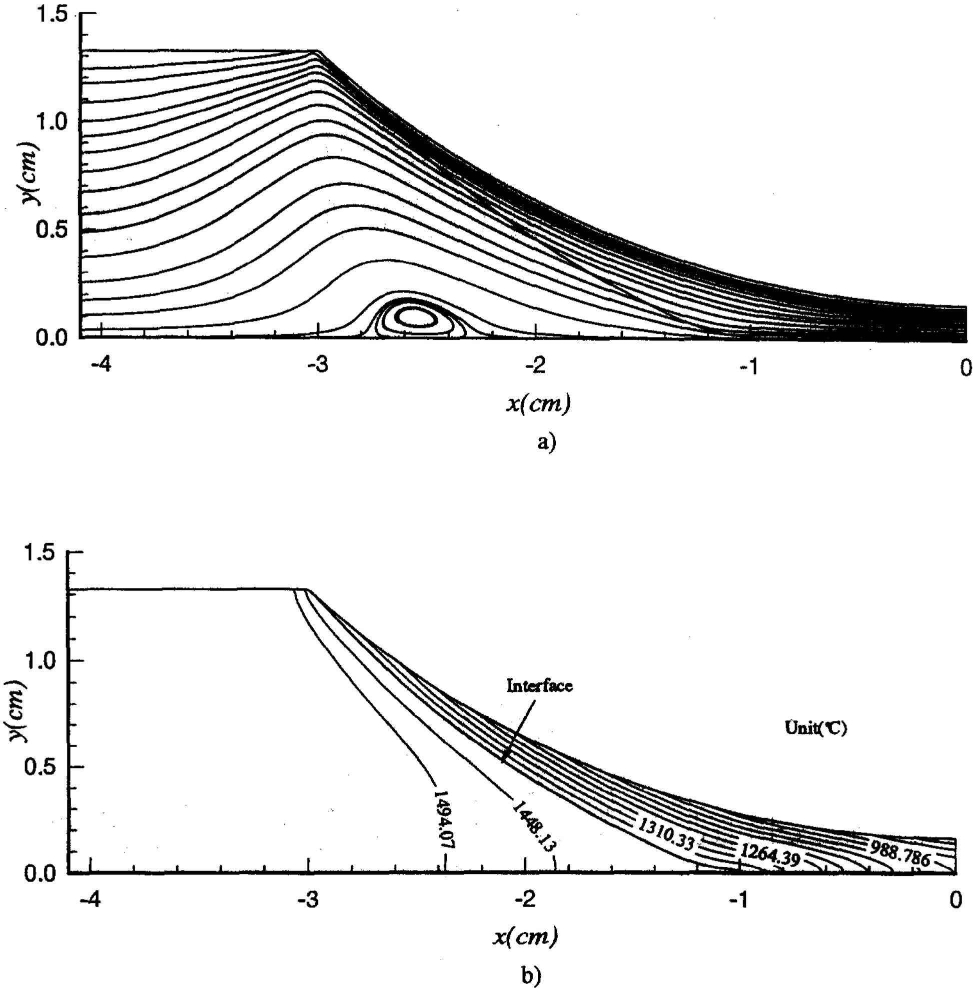

Fig. 7. Flow and temperature fields at $\omega = 0.27$ rad s^{-1}: (a) stream lines; (b) temperature contour.

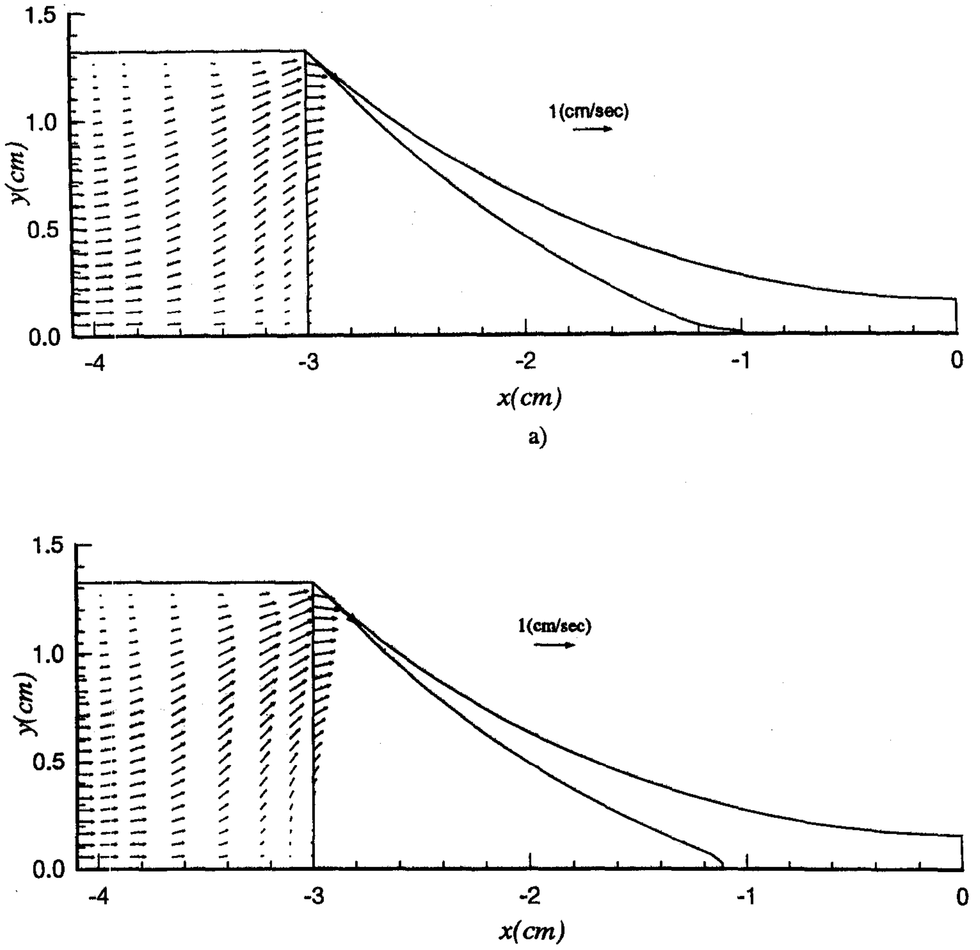

a)

b)

Fig. 8. Velocity vector in inlet region at (a) $\omega = 0.27$ rad s^{-1}; (b) $\omega = 0.36$ rad s^{-1}.

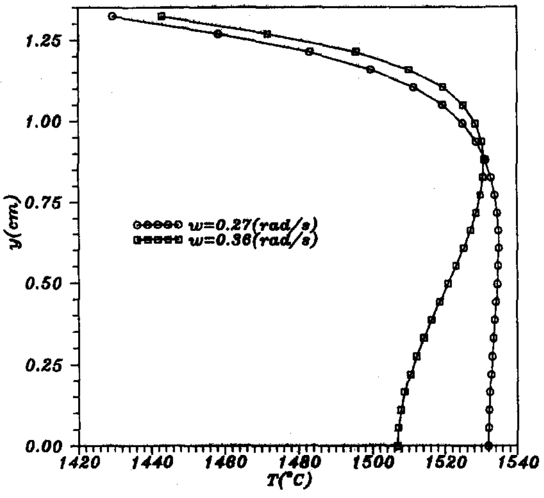

Fig. 9. Inlet temperature variation at $x = -3$ along height of inlet.

the efficiency of the heat transfer. Figure 13 shows the interface profiles at different ω, the interface position of upper strip surface moves forwards as ω increases. On the contrary, the interface position of midplane moves inwards as ω increases. The cause of this behavior is that the circulation makes the temperature field to be redistributed. In addition, the thickness of the solidified shell is also influenced by ω. As ω is

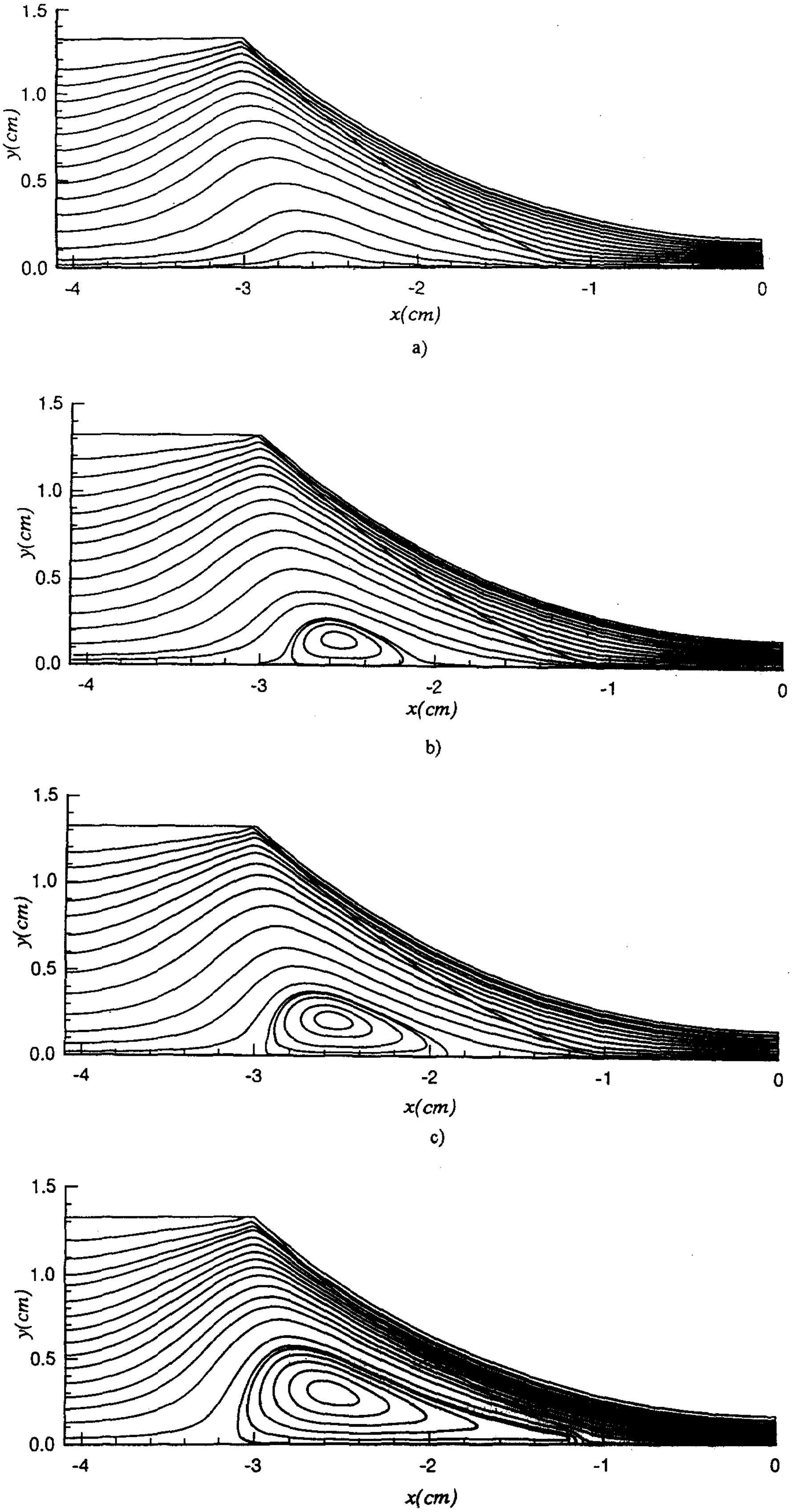

a)

b)

c)

d)

Fig. 10. Stream lines at (a) $\omega = 0.26$ rad s^{-1}; (b) $\omega = 0.28$ rad s^{-1}; (c) $\omega = 0.3$ rad s^{-1}; (d) $\omega = 0.36$ rad s^{-1}.

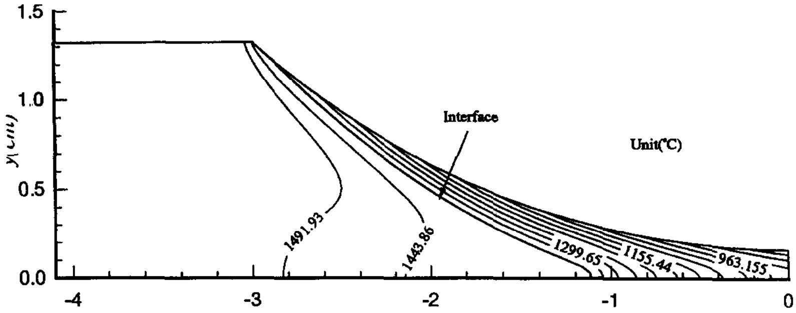

Fig. 11. Temperature contour at $\omega = 0.36$ rad s^{-1}.

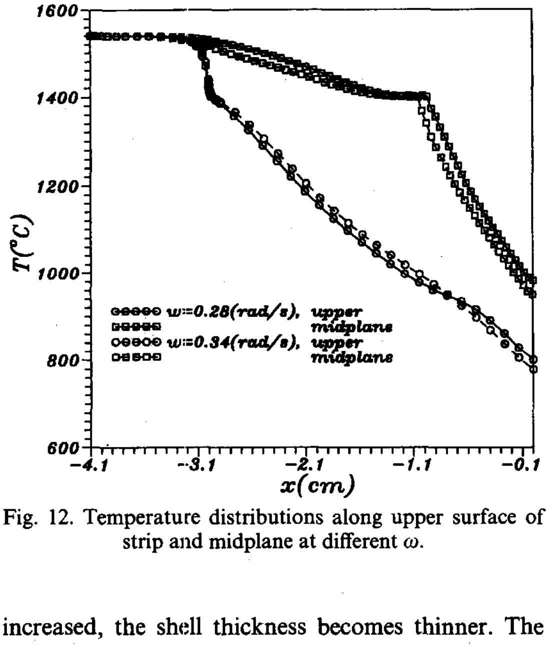

Fig. 12. Temperature distributions along upper surface of strip and midplane at different ω.

increased, the shell thickness becomes thinner. The influence of the flow rate on the interface position can be seen in the Fig. 14. As the flow rate is increased, the interface move toward the nip. From Figs. 13 and 14, these results also indicate that the interface shape, as well as the solidified position at midplane, is not only a function of ω, but also of flow rate, Q. Finally, Fig. 15 shows the temperature along the upper surface of the strip and midplane at different flow rates. As can be seen, the temperature increases as the flow rate is increased, since the larger flow contains more thermal energy needed to conduct outwards by the roller.

CONCLUDING REMARKS

The finite element method presented here provided a simple and efficient tool to simulate the twin-roll casting problem. The complexity of remesh phase of multidomain methods can largely reduce by incorporating the interface search scheme based on a local transform technique. Thus, the simulation of different materials behavior and the discontinuity of material properties can easily be handled. In addition, the solutions of the interface shape and the temperature, obtained near the interface, can provide more accuracy. The results from present study are summarized as follows:

(1) The inlet region must be included in the analysis, thus, the velocity conditions at the beginning of roll bite can be decided naturally. It also has the influence on the flow field within the strip.

(2) The velocity field is exhibited a two-dimensional behavior and it also has a significant influence on the temperature field.

(3) The circulation is driven mainly by the force convection and the circulation zone enlarges as the angular speed of the roller is increased.

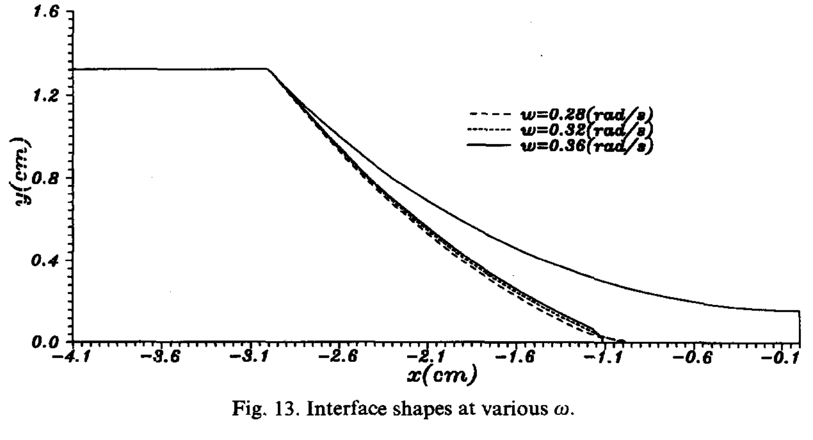

Fig. 13. Interface shapes at various ω.

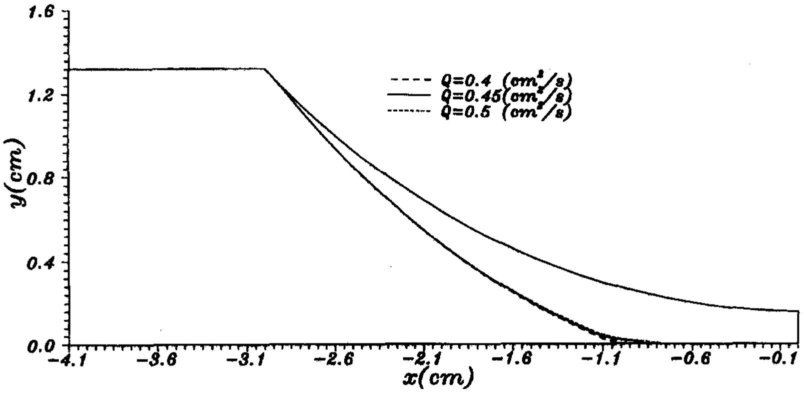

Fig. 14. Interface shapes at different flow rates and $\omega = 0.32$ rad s^{-1}.

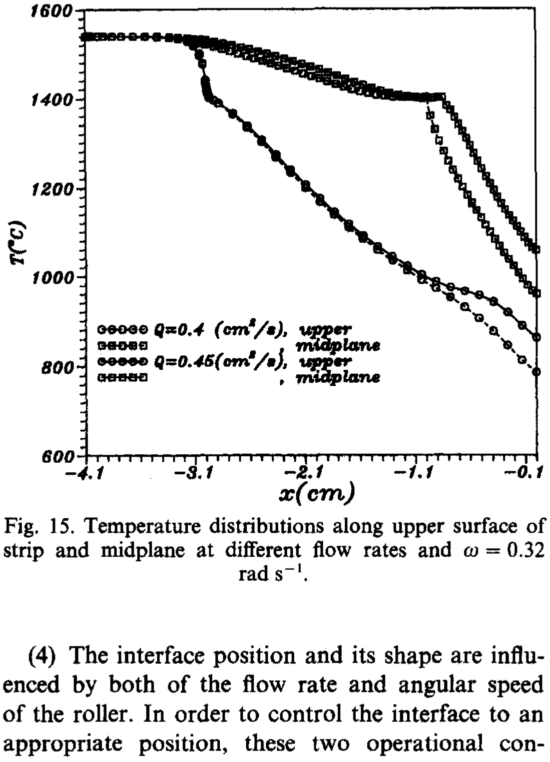

Fig. 15. Temperature distributions along upper surface of strip and midplane at different flow rates and $\omega = 0.32$ rad s^{-1}.

(4) The interface position and its shape are influenced by both of the flow rate and angular speed of the roller. In order to control the interface to an appropriate position, these two operational conditions must be considered simultaneously.

In this paper, we have been developed a general thermomechanical model as well as numerical algorithm to simulate the twin-roll process. One of the salient features of the present analysis is a more realistic representation of the fluid-flow phenomena in the molten metal as compared to some of the aforementioned literatures. However, some assumptions made in the formulation must be clarified from a more realistic aspect. The assumption of the large ratio of width to thickness is made and hence the complicated three-dimensional model can be reduced to the two-dimensional one. That assumption also implies that the obtained results are valid only in the cross-sections of width where are not near the side board. As a consequence, the flow pattern of the inlet condition is somewhat different from the fully developed profile of plane Poiseuille flow and the interface shape is three-dimensional when the side board effect is taken into account. Additionally, the effect of the mushy zone is neglected for simplifying the numerical treatment. However, the effect of which also has the influence on the flow and temperature fields mainly depending on the magnitude of the difference between the solidus and liquidus temperature and cooling condition. As deduced from the damped effect of the mushy zone, the circulation zone predicted by the present model may be somewhat larger than that in the actual situation. Finally, a further examination of the experimental data for accessing the deviation of the present model on the measurable quantity will be needed in the future.

REFERENCES

1. Shibuya, K. and Ozawa, M., Strip casting techniques for steel. *ISIJ International*, 1991, **31**, 661–668.
2. Büchner, A. R. and Schmitz, J. W., Thin-strip casting of steel with a twin-roll caster-discussion of product defects of ~1 mm-Fe6%Si-strips. *Steel Research*, 1992, **63**, 7–11.
3. Miyazawa, K. and Szekely, J., A mathematical model of splat cooling process using the twin-roll technique. *Metallurgy Transactions*, 1981, **12**, 1047–1057.
4. Saitoh, T., Hojo, H., Yaguchi, H. and Kang, C. G., Two-dimensional model for twin-roll casting. *Metallurgy Transactions B*, 1989, **20**, 381–390.
5. Karabin, M. E. and Smelser, R. E., A simplified thermomechanical model of roll casting. *ASME Winter Annual Meeting*, Miami Beach, Florida, 1985, pp. 17–21.
6. O'Malley, R. J., Karabin, M. E., and Smelser, R. E., The roll casting process: numerical and experimental results. *Journal of Materials Processing and Manufacturing Science*, 1994, **3**, 59–72.
7. Takuda, H., Hatta, N., Teramura, M. and Kokado, J., A simple model for thermal calculation in twin-roll strip casting process. *Steel Research*, 1990, **61**, 312–317.
8. Ha, M. Y., Kim, K., Kim, K. C. and Lee, S. W., Transient analysis of thermo-fluid phenomena in twin-roll continuous casting. *International Journal of Heat and Mass Transfer*, 1994, **37**, 2059–2068.
9. Hwang, J. D., Lin, H. J., Hwang, W. S. and Hu, C. T., Numerical simulation of metal flow and heat transfer during twin roll strip casting. *ISIJ International*, 1995, **35**, 170–177.
10. Hwang, S. M. and Kang, Y. H., Analysis of flow and

heat transfer in twin-roll strip casting by finite element method. *ASME Journal of the Engineering Industry*, 1995, **117**, 304–315.

11. Chang, J. G. and Weng, C. I., Numerical modelling of twin-roll casting by the coupled fluid flow and heat transfer model. *International Journal of Numerical Methods in Engineering*, 1997, **40**, 493–509.
12. Kroeger, P. G. and Ostrach, S., The solution of a two-dimensional freezing problem including convection effects in the liquid region. *International Journal of Heat and Mass Transfer*, 1974, **17**, 1191–1207.
13. Zienkiewicz, O. C., Flow formulation of numerical solution of forming process. In *Numerical Analysis of Forming Processes*, ed. J. F. T. Pittman, O. C. Zienkiewicz, R. D. Wood and J. M. Alexander, Chapter 1. Wiley, New York, 1984.
14. Zienkiewicz, O. C., Jain, P. C. and Onate, E., Flow of solids during forming and extrusion: some aspects of numerical solutions. *International Journal of Solids and Structures*, 1978, **14**, 15–38.
15. Kobayashi, S., Oh, S. and Altan, T., *Metal Forming and the Finite-Element Method*, Chapter 4. Oxford University Press, New York, 1989.
16. Altan, T. and Boulger, F. W., Flow stress of metals and its application in metal forming analysis. *ASME Journal of Engineering Industry*, 1973, **95**, 1009–1019.
17. Fujita, Y., Sato, H., Kitagawa, T., Nishioka, S., Tsuchida, Y. and Ozeki, A., Solidification and roll-bonding of shells in twin-roll casting process. *ISIJ International*, 1989, **29**, 495–502.
18. Sani, R., Gresho, P. M., Lee, R. L. and Griffiths, D. F., The cause and cure (?) of the spurious pressures generated by certain FEM solutions of the incompressible Navier–Stokes equations, Parts I and II. *International Journal of Numerical Methods of Fluids*, 1981, **1**, 17–43, 171–204.
19. Engelman, M. S., Sani, R. L., Gresho, P. M. and Bercovier, M., Consistent vs. reduced integration penalty methods for incompressible media using several old and new element. *International Journal of Numerical Methods of Fluids*, 1982, **2**, 25–42.
20. Kim, S. W. and Decker, R. A., Velocity-pressure integrated verse penalty finite element methods for high-Reynolds-number flows. *International Journal of Numerical Methods of Fluids*, 1989, **9**, 43–57.
21. Kim, S. W., A fine grid finite element computation of two-dimensional high Reynolds number flows. *Computers and Fluids*, 1988, **16**, 429–444.
22. Heinrich, J. C. and Zienkiewicz, O. C., Quadratic finite element schemes for two-dimensional convective transport problems. *International Journal of Numerical Methods of Engineering*, 1977, **11**, 1831–1844.
23. Huebner, K. H. and Thornton, E. A., *The Finite Element Method for Engineers*, Chapter 9. Wiley, New York, 1982.
24. Heinrich, J. C. and Marshall, R. S., Viscous incompressible flow by penalty function finite element method. *Computers and Fluids*, 1981, **9**, 73–83.
25. Pelletier, D., Fortin, A. and Camarero, R., Are FEM solutions of incompressible flows really incompressible? (or how simple flows can cause headaches!). *International Journal of Numerical Methods of Fluids*, 1989, **9**, 99–112.
26. Fortin, M. and Fortin, A., A generalization of Uzawa's algorithm for solution of Navier–Stokes equations. *Communications of Applied Numerical Methods*, 1985, **1**, 205–210.